

# Synthesis of Eu-doped bismuth germanate nano-ceramic powder

S. POLOSAN\*, E. MATEI, C. LOGOFATU

National Institute of Materials Physics, PO Box MG-7, Bucharest-Magurele, 77125, Romania

Europium doped  $\text{Bi}_4\text{Ge}_3\text{O}_{12}$  nanocrystals were successfully obtained by solid state reaction between precursor oxides at  $800^\circ\text{C}$ . The XRD and XPS measurements shows an increasing of the lattice constant in the case of Eu:BGO nanocrystals, due to the electropositive character of Eu(III) ions compared with the host cations, which induces an ionic character for Eu-O bound and a more covalent one for the Ge-O bounds. The photoluminescence of Eu:BGO due to  ${}^5\text{D}_0 \rightarrow {}^7\text{F}_2$  transition have a lower splitting compared with Eu:BGO monocrystals suggesting a lower crystal field in the sintered nanocrystals, due to a mixing between the crystalline and amorphous phases.

(Received July 24, 2010; accepted October 14, 2010)

*Keywords:* Powders-solid state reaction, Grain size, Spectroscopy, Mixing

## 1. Introduction

Ceramic phosphors become nowadays an important constituent for the scintillating materials. From this class of materials some new optical materials like  $\text{Lu}_2\text{O}_3:\text{Eu}$  nanocrystals based  $\text{SiO}_2$  sol-gel materials and nanocrystalline cerium silicates are reported [1-3]. Those nano-ceramics exhibits intense luminescence at room temperature, fulfilling at least two main attributes of scintillating materials: high luminescence and room temperature measurements.

In the first case, the fluorescence of  $\text{Lu}_2\text{O}_3:\text{Eu}$  nanocrystals based  $\text{SiO}_2$  were studied versus thermal treatments. After sintering at  $1250^\circ\text{C}$ , the fluorescence lifetime increases at about 1.5 ms even at room temperature, and their high fluorescence recommending this material for display applications together with scintillating detectors.

In the second case, the nanocrystallite  $\text{CeO}_2$  based  $\text{SiO}_2$  of about 5 nm after  $900\text{-}1050^\circ\text{C}$  heat treatments, exhibit strong luminescence in the range of 350-500 nm with two peaks at 410 nm and 490 nm.

Among the scintillating materials, the  $\text{Bi}_4\text{Ge}_3\text{O}_{12}$  (BGO) crystals become a good scintillator because of their high density of around  $7.13\text{ g/cm}^3$ , which is the third requirement for a good scintillator, ensuring a short length of scintillation. Unfortunately, the crystal growth procedure is quite complicate because  $\text{Bi}_2\text{O}_3$  has a lower melting point ( $823^\circ\text{C}$  vs  $1050^\circ\text{C}$ ) compared with  $\text{GeO}_2$  powder and requests special conditions [4,5]. BGO scintillators can also be obtained as glass-ceramic materials, with good scintillating properties under electrons and X-ray irradiation [6,7]. Bismuth germanates, as ceramic powders, can also be obtained by Pechini method starting with bismuth and germanium oxides as precursors [8, 27].

The  $\text{GeO}_2$  is known as a “glass former” and can be seen as a polymer structure due to the formation of  $\text{GeO}_4$  tetrahedra which connect the other compounds [9]. This is the reason why the properties of these materials are closely connected with the presence and movement of  $\text{GeO}_4$  structures. The existence of independent  $\text{GeO}_4$  “tetrahedra” and  $\text{Bi}^{3+}$  ions in the melt was shown by the Raman spectra recorded on BGO crystals at higher temperatures (slightly above the melting point of the crystal) [10].

However, the scintillation mechanism in BGO materials is based on an intrinsic photoluminescence of  $\text{Bi}^{3+}$  ions due to the  $6s6p \rightarrow 6s^2$  transition under UV or X-ray radiation [11,12]. This photoluminescence has a long lifetime of about 300 ns at room temperature, but in BGO polycrystalline powder, the decay constants, especially the fast one of about 100 ns at 10 K, suggest different mechanisms of energy absorption and transfer to the  $\text{Bi}^{3+}$  ions [11,13].

The aim of this paper is the synthesis and structural characterization of Eu-doped  $\text{Bi}_4\text{Ge}_3\text{O}_{12}$  (further called Eu:BGO) nano-ceramics, obtained by solid state reaction. The  $\text{Eu}^{3+}$  ions are used as a probe in these studies of crystallization, because of their high photoluminescence and sensitivity to the crystalline environment. The methods of characterization XRD, SEM, EDX, FTIR, Raman, photoluminescence and XPS measurements has been used in order to investigate the properties of BGO nanocrystals.

## 2. Experimental

In the first step mixtures of 40%  $\text{Bi}_2\text{O}_3$ , 59%  $\text{GeO}_2$  and 1%  $\text{Eu}_2\text{O}_3$  (in molar percents) have been wet-mixed in acetone, dried at  $100^\circ\text{C}$  for 24 h and transferred to an  $\text{Al}_2\text{O}_3$  crucible, and then heated at  $800^\circ\text{C}$  for 6 h in order to accomplish the chemical reaction, called Solid State

Reaction (SSR). Then the mixtures have been slowly quenched to the room temperature. The resulted ceramic powder was compared with the BGO commercial powder from Merk.

The phases and crystallinity of these phases were analyzed by X-ray diffraction (XRD) using a Bruker D8 Advance equipment with Cu  $K_{\alpha}$  radiation. The slit was set at 0.2 mm. The mean crystallite size was determined using the Scherrer formula:

$$D = \frac{k\lambda}{\cos\theta * \sqrt{\beta^2 - \beta_o^2}}$$

where  $\beta$  is the half-width (in degree) of diffraction line,  $\beta_o$  a half-width of the reference line (instrumental broadening),  $\lambda$  is the wavelength of the X-rays ( $\lambda_{CuK\alpha1}=1.5406 \text{ \AA}$ ),  $\theta$  is the Bragg angle, and  $k$  is a constant related to the crystallite shape taken as  $k=0.89$ . After corrections, the half-width is converted in radians. The analysis was performed on the basis of the [310] reflection in XRD pattern ( $2\theta=26.76^\circ$ ), assuming that the whole line broadening of the sample originates from the small crystallite size. The line width was determined after subtraction of  $K_{\alpha2}$  lines from the  $K_{\alpha1}$ - $K_{\alpha2}$  doublet, by the Rachinger algorithm, using the Bruker Difrac<sup>plus</sup> Basic Evaluation program package [14].

We employed a Zeiss EVO 50 SEM with LaB<sub>6</sub> cathode with Bruker EDX system. Based on the SEM images, the equipment can generate secondary electrons, back scattered electrons, characteristic X-ray and chatodoluminescence.

The Raman spectra have been recorded on bulk glass samples with a Jasco NRS-3100 spectrometer, from 100 to 1000  $\text{cm}^{-1}$ , using 785 nm laser.

The photoluminescence spectra were recorded with Edinburgh F910 fluorimeter.

Infrared spectra have been recorded at room temperature with a Jasco FT-IR FT/IR-6200 type A spectrometer with a TGS detector, between 7000-350  $\text{cm}^{-1}$ . The scan speed was set at 2 mm/s and the resolution at 2  $\text{cm}^{-1}$ .

The X-ray photoemission spectroscopy (XPS) spectra were taken with a VG ESCA 2 MkII spectrometer using the  $Al_{K\alpha}$  radiation (1486.6 eV), 250 W, with a resolution of 20 eV and 256 recording channels.

The sample was positioned at  $55^\circ$  in respect to the analyzer axis and the pressure in the analysis chamber was held at  $10^{-9}$  mbar. The XPS registered spectra were processed using the Spectral Data Processor V3.2 (SDP) software.

### 3. Results

From the Fig. 1, there are additional crystallographic phases formed together BGO structure, very probable  $Bi_2GeO_5$  and  $Bi_{12}GeO_{20}$ . The d-spacing and some identification for these phases are presented in the Table 1.

The analysis of the BGO crystalline dimensions were done by using the [310] reflection from around  $2\theta=26.74^\circ$ , because this is the first line which appears at the

crystallization process. Similar behaviour was obtained in deposited BGO thin film by thermal evaporation [15]. In the complete amorphous state there are two large peaks, one at  $2\theta=29^\circ$  which is the mark of the scattering on the BGO nanocrystals and another one at  $2\theta=55^\circ$  which is due to the residual phase [7]. As one may see in the inset, there is a shift between the Eu:BGO and the BGO Merk powder of about  $0.0368^\circ$ .

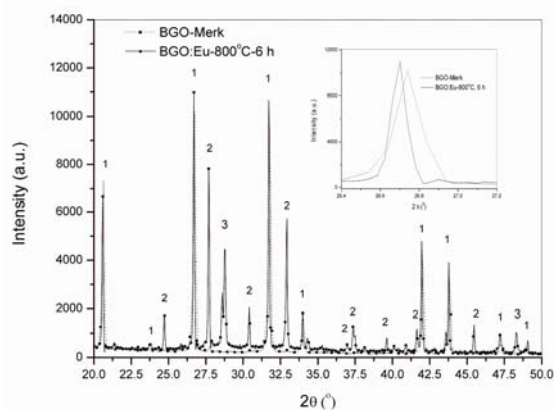


Fig. 1. X-ray diffraction of Eu:BGO (straight line) and BGO Merk powder (dotted line): 1-  $Bi_4Ge_3O_{12}$  phase, 2-  $Bi_2GeO_5$  phase, 3-  $Bi_{12}GeO_{20}$  phase.

The assignment of selected peaks in the XRD pattern is listed in the table 1 (d-spacing), together with their crystalline phases and planes. As we can see, in Eu:BGO sample, aside of  $Bi_4Ge_3O_{12}$  other two compounds are formed mainly  $Bi_{12}GeO_{20}$ ,  $Bi_2GeO_5$  and even  $GeO_2$  ( $2\theta=28.55^\circ$ , [222]).

Table 1. Selective d-spacing for Eu:BGO and BGO.

Eu:BGO d-spacing	BGO d-spacing	Index
4.3099	4.2985	$Bi_4GeO_{12}$ [211]
3.5970		$Bi_{12}GeO_{20}$ [220]
3.3357	3.3312	$Bi_4GeO_{12}$ [310]
3.2192		$Bi_{12}GeO_{20}$ [310]
3.1024		$Bi_2GeO_5$ [311]
2.9371		$Bi_{12}GeO_{20}$ [222]
2.8195	2.8174	$Bi_4GeO_{12}$ [321]
2.7200		$Bi_2GeO_5$ [020]
2.6349	2.6323	$Bi_4GeO_{12}$ [400]

The calculated grain size of the Eu:BGO nanocrystals from the [310] reflection was found to be 35 nm, compare with the BGO Merk powder which have a grain size of about 62 nm.

SEM images of BGO Merk powder and Eu:BGO nanoparticles are presented in the Fig. 2. The morphology of Eu:BGO sample do not differ too much compared with BGO Merk except the dimensions of nanoparticles which are almost double in the size for the last case, confirming

the XRD calculations following Debye-Scherer method. The form of the particles looks very similar, even if the whole grain is higher.

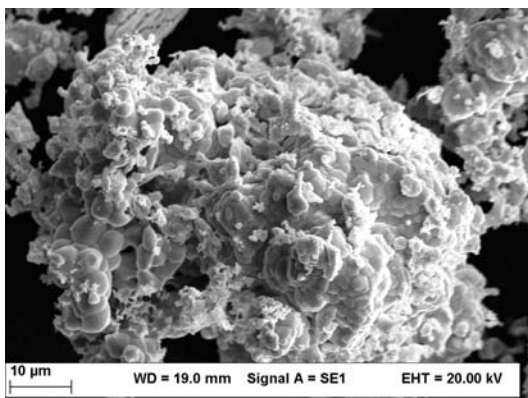


Fig. 2. SEM images of Eu:BGO.

The EDX graphs of commercial  $\text{Bi}_4\text{Ge}_3\text{O}_{12}$ -Merk and Eu:  $\text{Bi}_4\text{Ge}_3\text{O}_{12}$  nanopowders (Fig. 3) are practically overlapped, except the region around 1.2 keV where the Ge have an energy of 1.19 keV and the Eu have an energy of 1.14 keV, practically under the bandwidth of the electrons beam. However the intensity of Eu is higher (almost 5 times) and the compositional analysis preserve the level of each ion (except the oxygen) and confirm a level of dopant of about 1-2% (see the Table 2).

Table 2. Compositions (in weight %) from EDX analysis.

Element	$\text{Bi}_4\text{Ge}_3\text{O}_{12}$ (wt.%)	Error (%)	Eu: $\text{Bi}_4\text{Ge}_3\text{O}_{12}$ (wt.%)	Error (%)
Germanium	21.64 (K)	0.7	22.04 (K)	0.7
Bismuth	63.15 (L)	2.0	63.55 (L)	2.0
Oxygen	15.17 (K)	0.9	13.22 (K)	2.3
Europium	-		1.15 (L)	0.1

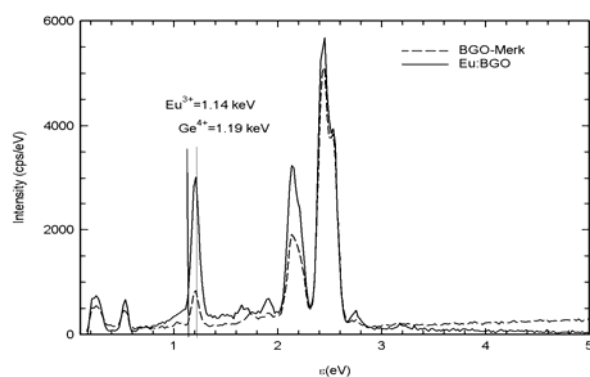


Fig. 3. EDX spectra of Eu:BGO and BGO Merk nano-powders.

The FTIR measurements (Fig. 4) on Eu:BGO powder shows a series of bands which are listed in Table 3. The high frequencies, from  $780\text{ cm}^{-1}$ ,  $730\text{ cm}^{-1}$  and  $701\text{ cm}^{-1}$ , has been assigned to the Ge-O vibrations type  $F_2$  in  $\text{Bi}_4\text{Ge}_3\text{O}_{12}$  (BGO). The frequencies between  $480\text{ cm}^{-1}$  and  $700\text{ cm}^{-1}$ , have been assigned to the Ge-O vibrations in  $\text{Bi}_4\text{Ge}_3\text{O}_{12}$ .

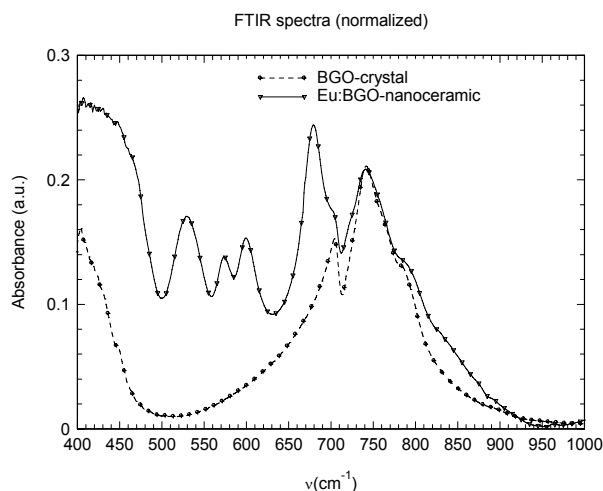


Fig. 4. FTIR spectra of Eu:BGO and BGO Merk nano-powders.

In the Fig. 5, the Raman spectrum of Eu:BGO is compared with the Raman spectrum of BGO powder. The peak positions for BGO are in good agreement with those in the BGO crystal [7].

The frequencies at  $625\text{ cm}^{-1}$ ,  $542\text{ cm}^{-1}$ ,  $327\text{ cm}^{-1}$  and  $238\text{ cm}^{-1}$  are assigned to  $\text{Bi}_{12}\text{GeO}_{20}$  nanocrystals.

Photoluminescence measurements were performed on the powder after solid state reaction by excitation at 394 nm which correspond to  ${}^7F_0 \rightarrow {}^5L_6$  transition of  $\text{Eu}^{3+}$  ions electric dipole interaction (Fig. 6). The main peaks are ascribed to  ${}^5D_0 \rightarrow {}^7F_0$  at 578 nm,  ${}^5D_0 \rightarrow {}^7F_1$  at 588 nm and the electric dipole allowed transition  ${}^5D_0 \rightarrow {}^7F_2$  ( $\Delta J=+2$ ) which is very sensitive to the crystal field around  $\text{Eu}^{3+}$  ions.

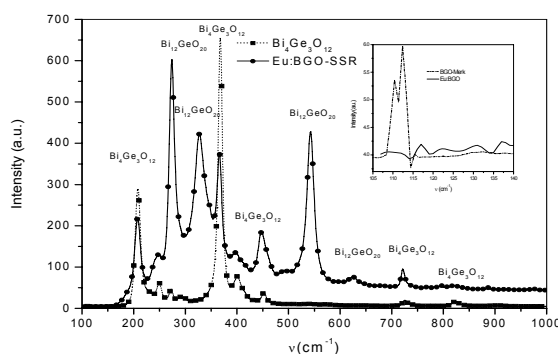


Fig. 5. Raman spectra of Eu:BGO and BGO Merk powder. The inlet shows an enlargement of the low frequency patterns.

The splitting is lower in the Eu:BGO nanoparticles compared with Eu:BGO monocrystal, suggesting a lower crystal field in BGO nanoparticles. Very important is the high intensity of the  $^5D_0 \rightarrow ^7F_4$  transition from 700 nm in the  $\text{Eu:Bi}_4\text{GeO}_{12}$  which gives important information about the host composition [22].

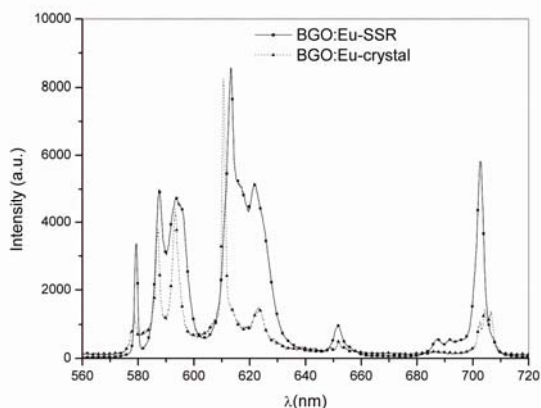


Fig. 6. Photoluminescence spectra of Eu:BGO and BGO Merck powders, excited at  $\lambda=394$  nm.

Excitation spectra of Eu:BGO nanoparticles by monitoring the photoluminescence of  $^5D_2 \rightarrow ^7F_0$  transition, is shown in the Fig. 7. The enlarged excitation spectra closed to 464 nm ( $21500\text{ cm}^{-1}$ ) which is due to the charge transfer to  $\text{Eu}^{3+}$  ions, shows at least two maxima at around  $355\text{ cm}^{-1}$  and  $820\text{ cm}^{-1}$  which were ascribed to the phonon side bands (PSB). The first peak is somehow asymmetric and a deconvolution of the first PSB peak shows two maxima at  $270\text{ cm}^{-1}$  and another to  $360\text{ cm}^{-1}$ . The most interesting is the peak from  $820\text{ cm}^{-1}$  which can be explained by the multiphonon relaxation processes in the oxide glasses [23].

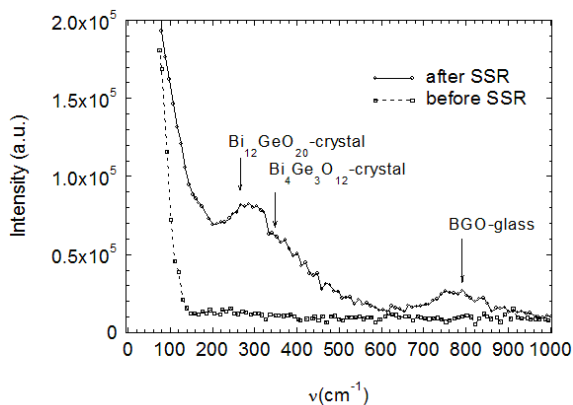


Fig. 7. Excitation spectra for the  $\lambda = 620$  nm photoluminescence by monitoring the  $\lambda = 464$  nm excitation band at high energy part.

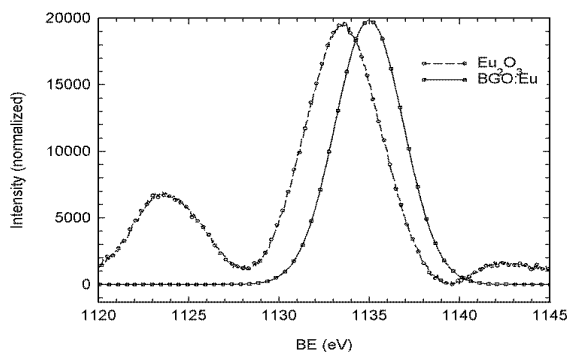


Fig. 8. XPS spectra of Eu:BGO and  $\text{Eu}_2\text{O}_3$  powder, by monitoring  $\text{Eu}_{3d_{5/2}}$  state.

Concerning the XPS measurements, the Eu:BGO spectrum shows a broad band around 1135 eV binding energy compared with the  $\text{Eu}_2\text{O}_3$  spectrum which shows at least one peaks at 1123.5 eV, besides the main one at 1133.7 eV. These spectra were obtained by monitoring the Binding Energy (BE) of  $\text{Eu}_{3d_{5/2}}$  states in the range of 1120-1145 eV for  $\text{Eu}_2\text{O}_3$  and Eu:BGO powder. The Eu-ions are lanthanide type with incomplete 4f subshells which exhibits splitting into several separate signals, beside the main photoelectron peak of  $\text{Eu}^{3+}$ . Those peaks are called shake-down satellites and are due to an apparent change in the 4f-subshell occupation number [26].

#### 4. Discussion

The shift of the [311] peak from the XRD patterns, induces an increasing of the of the lattice constant from  $10.51\text{ \AA}$  in BGO Merck powder to  $10.54\text{ \AA}$  for Eu:BGO powder. This fact is similar with the  $\text{Eu}^{3+}$ -ion incorporation inside the  $\text{CaF}_2$  nanocrystals and can be explained by the changing of the 6-fold coordination by replacing  $\text{Bi}^{3+}$  with  $\text{Eu}^{3+}$  ions [16,17]. The radius of  $\text{Eu}^{3+}$  ions in octahedral symmetry is  $0.109\text{ nm}$  and for  $\text{Bi}^{3+}$  is  $0.117\text{ nm}$  which normally leads to the decreasing of the lattice constant. The increasing of this parameter could be explained as follow: the  $\text{O}^{2-}$  ions are attracted toward the cations of the host glass (in these case, Ge ions) by the Coulomb attractive force because the  $\text{Eu}^{3+}$  is electropositive compared with the other cations of the host. Hence, the radius of the  $\text{Eu}^{3+}$  ion can be enlarged when the host is a combination between glass and nanocrystals. This is consistent with the XPS measurements as we will see below. From the phonon-side bands measurements there are a residual amorphous phase which influences the properties of Eu:BGO nanocrystals.

It is very interesting to note that the solid state reaction between only  $\text{Bi}_2\text{O}_3$  and  $\text{GeO}_2$  goes directly to  $\text{Bi}_4\text{GeO}_{12}$  and, from BGO amorphous materials, by recrystallization, have an intermediate phase  $\text{Bi}_2\text{GeO}_5$  [7, 28]. By solid state reaction of  $\text{Bi}_2\text{O}_3$  and  $\text{GeO}_2$  but mixed with  $\text{Eu}_2\text{O}_3$  (1-2%) result a multi-phase ceramic powder which include also  $\text{Bi}_{12}\text{GeO}_{20}$ . Taking into account the first six XRD peaks between  $24^\circ$  to  $55^\circ$ , the calculated lattice constant for  $\text{Bi}_{12}\text{GeO}_{20}$  cubic structure is  $10.1435$  and a

volume of 1043.67, in a good agreement with the JCPDS database for the  $\text{Bi}_{12}\text{GeO}_{20}$  structure (PDF# 77-0861) which gives a lattice constant of 10.153 and a volume of 1046.61.

BGO belongs to I43d space group with four formula units in the crystallographic unit-cell. The factor group analysis yields to 27 Raman active modes and 14 infrared active modes [9]:

$$\Gamma=4A_1+5A_2+9E+14F_1+14F_2$$

For the frequency range between 700 -500  $\text{cm}^{-1}$ , there are at least four frequencies peaked at 680  $\text{cm}^{-1}$ , 607  $\text{cm}^{-1}$ , 580  $\text{cm}^{-1}$  and 530  $\text{cm}^{-1}$  which belongs to  $\text{Bi}_{12}\text{GeO}_{20}$  structure. As shoulders, another two frequencies appears at 830  $\text{cm}^{-1}$  and 480  $\text{cm}^{-1}$ . The space group I23 and the factor group analysis yields to:

$$\Gamma=8A+8E+25F$$

Among them the F modes are active infrared and some frequencies were found at 679  $\text{cm}^{-1}$ , 598  $\text{cm}^{-1}$ , 578  $\text{cm}^{-1}$ , 526  $\text{cm}^{-1}$  and 493  $\text{cm}^{-1}$  [18].

The Raman vibrations below 360  $\text{cm}^{-1}$  for the BGO structure are assigned to the motion of whole tetrahedral groups against the  $\text{Bi}^{3+}$  sublattice. Above 360  $\text{cm}^{-1}$  the peaks are assigned to the vibrations of the  $\text{GeO}_4$  units; the main peak at 364  $\text{cm}^{-1}$  is due to the degenerate  $\nu_2$ ,  $\nu_4$  bending vibrations of the  $\text{GeO}_4$  "tetrahedra". The small peaks at 724 and 820  $\text{cm}^{-1}$  are assigned to  $\nu_1(\text{GeO}_4)$  vibrations having different symmetries.

The first two peaks of  $\text{Bi}_{12}\text{GeO}_{20}$  structure correspond to the asymmetric stretching modes of four Bi-O bonds with different lengths and the last two frequencies correspond to transitions and rotation modes of  $\text{GeO}_4$  units [19, 20]. This fact was observed also in the BGO thin films obtained by Pechini method, using Raman technique [24]. A closed view of the Raman spectra shows a vibration at 112  $\text{cm}^{-1}$  in  $\text{Bi}_4\text{GeO}_{12}$  crystal assigned to Bi-O vibration which decreases in the Eu:BGO Raman spectrum, similar with the case of Eu: $\text{Bi}_4\text{Ti}_3\text{O}_{12}$  [21].

In the amorphous materials, variations in the  $\text{Eu}^{3+}$  photoluminescence spectrum are considered to be restricted to differences in the intensities of the  ${}^5\text{D}_0 \rightarrow {}^7\text{F}_2$  and  ${}^5\text{D}_0 \rightarrow {}^7\text{F}_4$  bands, which depend on the Judd-Ofelt parameters  $\Omega_2$  and  $\Omega_4$  respectively. The  ${}^5\text{D}_0 \rightarrow {}^7\text{F}_4$  intensity ( $\Omega_4$ ) seems to depend mainly on long-range effects (related to bulk properties of the glass) suggesting the residual phase of Eu:  $\text{Bi}_4\text{GeO}_{12}$ .

When the energy gaps between the excited states, in this case  ${}^5\text{D}_0$  and the next  ${}^7\text{F}_j$  lower states is larger than the maximum phonon energy of the host material, emission of several phonons is requested due to the energy conservation law. Since the highest-energy phonons can conserve the energy in the lowest-order process, they play the important role in the relaxation processes. A theory which connects the phonon-side bands with the local structure around  $\text{Eu}^{3+}$  ions was developed [24]. This fact can be done by monitoring the  ${}^5\text{D}_0 \rightarrow {}^7\text{F}_2$  emission into the excitation spectra aside a pure electronic transition, in this

case  ${}^5\text{F}_0 \rightarrow {}^7\text{D}_2$  because the next level  ${}^5\text{L}_6$  is far enough (over 2000  $\text{cm}^{-1}$ ) and it is known that for the oxide glasses, the highest frequency vibrations are between 700 to 1400  $\text{cm}^{-1}$ . Because the PSB bands are generally uniform broadened, it was concluded that the coupling can be done only by the stretching vibrations. In the  $\text{GeO}_2$ -based glasses, the highest frequency Raman mode was determined at 818  $\text{cm}^{-1}$ , in our case at 823  $\text{cm}^{-1}$ . The assignment of the 810-820  $\text{cm}^{-1}$  from the Fig. 7, marks the weakly coupling of  $\text{Eu}^{3+}$  ions with the surrounding network and hence the existence of the amorphous BGO structure. Because the rate of multiphonon processes is host dependent, when the crystallization process around  $\text{Eu}^{3+}$  ions, the coupling is realized by the optical phonons of the crystal field. The  $\text{GeO}_4$  tetrahedra began a stable process or rearranging and forms the  $\text{Bi}_4\text{Ge}_3\text{O}_{12}$  and  $\text{Bi}_{12}\text{GeO}_{20}$  crystalline structures. In the crystalline phases, the weak coupling from the glass phase becomes strong coupled by rearranging of  $\text{GeO}_4$  tetrahedra. This fact is similar with the case of  $\text{PbF}_2$  formation in the Eu-doped  $\text{SiO}_2$ - $\text{PbF}_2$  glasses [25]. From the Raman spectra we can see the appearance of 357  $\text{cm}^{-1}$  mode for the  $\text{Bi}_4\text{Ge}_3\text{O}_{12}$  and 270  $\text{cm}^{-1}$  mode for the  $\text{Bi}_{12}\text{GeO}_{20}$  due to the reduction symmetry of  $\text{GeO}_4$  tetrahedra [19]. The two peaks from 270  $\text{cm}^{-1}$  and 360  $\text{cm}^{-1}$  from the PSB spectrum of Eu:BGO nanocrystals should be assigned to the phonon coupling of the  $\text{Eu}^{3+}$  ions with two structures  $\text{Bi}_4\text{Ge}_3\text{O}_{12}$  and  $\text{Bi}_{12}\text{GeO}_{20}$ .

The exploitation of XPS satellites determines the chemical environment of the  $\text{Eu}^{3+}$  ions. The low values of those shake-down satellites, in the case of Eu:BGO powder, together with the energy shift of the Binding Energy (BE) with about 1.3 eV, suggests different environment of the  $\text{Eu}^{3+}$  compared with  $\text{Eu}_2\text{O}_3$  powder. In fact,  $\text{Eu}^{3+}$  is the most electropositive element in the complex Eu-O-Ge, having the electronegativity 1.2 on the Pauling scale, compared with 2.01 for Ge ions. Consecutively, the Ge-O bounds are more covalent than Eu-O bounds which pull away the electrons from Eu, giving a more ionic character for the Eu-O bound and inducing an increasing of core-level BE of  $\text{Eu}^{3+}$ . This fact is consistent with the increasing of lattice constant of Eu:BGO nanocrystals, compared with BGO-Merk crystalline powder.

## 5. Conclusions

Europium doped BGO nanocrystals were successfully obtained by solid state reaction between precursor oxides at 800°C.  $\text{Eu}^{3+}$  ions were used as a probe for studying the crystallization processes which take a place during solid state reaction. Compared with undoped solid state reaction between  $\text{Bi}_2\text{O}_3$  and  $\text{GeO}_2$  powders, in the case of Eu-doped germanates, beside BGO, two new phases appears:  $\text{Bi}_2\text{GeO}_5$  and  $\text{Bi}_{12}\text{GeO}_{20}$ .

The XRD and XPS measurements shows an increasing of the lattice constant in the case of Eu:BGO nanocrystals, due to the electropositive character of Eu(III) ions compared with the host cations, which induces an ionic character for Eu-O and Ge-O bounds becomes more covalent.

The sintered Eu:BGO powder have a larger dimension compared with the pure BGO powder, suggesting a heteronucleation process accomplished by the  $\text{Eu}^{3+}$  ions.

The photoluminescence of Eu:BGO due to  $^5\text{D}_0 \rightarrow ^7\text{F}_2$  transition have a lower splitting compared with Eu:BGO monocrystals suggesting a lower crystal field in the sintered nanocrystals. In the case of  $^5\text{D}_0 \rightarrow ^7\text{F}_4$  transition intensity, related to the  $^5\text{D}_0 \rightarrow ^7\text{F}_2$  transition intensity, seems to depend mainly on long-range effects (related to bulk properties of the glass) suggesting the amorphous residual phase of Eu:  $\text{Bi}_4\text{GeO}_{12}$ , besides the crystalline structures.

### Acknowledgments

The authors gratefully acknowledge the financial support of the Romanian Ministry of Education and Research (PN II Project 71-007 / 2007).

### References

- [1] D. Hreniak, E. Zych, L. Kepinski, W. Streck, *J. Phys. Chem. Sol.* **64**, 111 (2003).
- [2] L. Kepinski, D. Hreniak, W. Streck, *J. Alloys Comp.* **341**, 203 (2002).
- [3] S. Polosan, C.E. Secu, *J. Optoelectron. Adv. Mat.* **10(8)**, 2134 (2008).
- [4] P. H. Sangeeta, S. C. Sabharwal, *J. Crystal Growth* **118**, 396 (1992).
- [5] S. Polosan et al., *Phys. Stat. Sol. C* **2(1)**, 93 (2005).
- [6] S. Polosan, M. Secu, *Rad. Meas.* **45**, 409 (2010).
- [7] S. Polosan, *J. Non-Cryst. Sol.* **355**, 1900 (2009).
- [8] F. A. Andrade de Jesus, R. S. da Silva, Z. S. Macedo, *J. Therm. Anal. Calorim.* **100(2)**, 537 (2010).
- [9] M. Couzi, J. R. Vignalou, G. Boulon, *Sol. State Comm.* **20**, 461 (1976).
- [10] X. Zhang, S. T. Yin, S. M. Wan, J. L. You, H. Chen, S. J. Zhao, Q. L. Zhang, *Chin. Phys. Lett.* **24**, 1898 (2007).
- [11] Y. P. Chapman, E. B. Courchesne, S. E. Derenzo, *J. of Lum.* **128**, 87 (2008).
- [12] S. Polosan, *Mat. Res. Bull.* **45**, 1492 (2010).
- [13] C. E. W. van Eijk, *Phys. Med. Biol.* **47**, R85 (2002).
- [14] W. A. Rachinger, *J. Sci. Instrum.* **25**, 254 (1948).
- [15] K. Arshak, O. Korostynska, J. Harris, D. Morris, A. Arshak, E. Jafer, *Thin Solid Films*, **516**, 1493 (2008).
- [16] F. Wang, X. Fan, D. Pi, M. Wang, *Sol. State Comm.*, **133**, 775 (2005).
- [17] Y. Kishi, S. Tanabe, S. Tochino, G. Pezzotti, *J. Am. Ceram. Soc.* **88**, 3423 (2005).
- [18] A. Golubovich, R. Gajic, C. Chen, A. Valcic, *Hemijska Ind.* **54**, 530 (2000).
- [19] M. Kamran, D. Yao-Min, M. Ji-Yun, L. Bo-Hong, H. Shi-Kun, Z. Wei-Jun, Z. Xiao-Rui, Q. Xiang-Gang, *Chinese Physics B*, **18(10)**, 4425 (2009).
- [20] A. V. Egorysheva, V. I. Burkov, V. S. Gorelik, Y. F. Kargin, A. V. Chervyakov, *Cryst. Rep.* **46(3)**, 461 (2001).
- [21] F. Camacho-Alanís, M. E. Villafuerte-Castrejón, G. González, A. Ibarra-Palos, J. Ocotlán-Flores, R. Y. Sato-Berrú, J. M. Saniger, M. Villegas, J. F. Fernández, *Ferroelectrics*, **339**, 191 (2006).
- [22] E. W. J. L. Oomen, A. M. A. van Dongen, *J. Non-Cryst. Sol.* **111**, 205 (1989).
- [23] C. B. Layne, W. H. Lowdermilk, M. J. Weber, *Phys. Rev. B*, **16(1)**, 10 (1977).
- [24] S. Todoroki, K. Hirao, N. Soga, *J. Ceram. Soc. Jap.* **101(9)**, 1065 (1993).
- [25] D. Zhao, X. Qiao, X. Fan, M. Wang, *Physica B*, **395**, 10 (2007).
- [26] F. Mercier, C. Alliot, L. Bion, N. Thommat, P. Toulhoat, *J. of El. Spect. & Rel. Phenom.* **150(1)** 21 (2006).
- [27] F. A. A. de Jesus, M. R. B. Andreetta, A. C. Hernandez, Z. S. Macedo, *Opt. Mat.* **32(10)**, 1286 (2010).
- [28] C. Berbecaru, H. V. Alexandru, S. Polosan, *Phys. Stat. Sol. (c)* **7(9)**, 2336 (2010).

\*Corresponding author: silv@infim.ro